

# SCIENTIFIC REPORTS



OPEN

## One-step synthesis of Nickel Iron-layered double hydroxide/reduced graphene oxide/carbon nanofibres composite as electrode materials for asymmetric supercapacitor

Feifei Wang, Ting Wang, Shiguo Sun, Yongqian Xu, Ruijin Yu &amp; Hongjuan Li

A novel NiFe-LDH/RGO/CNFs composite was produced by using a facile one-step hydrothermal method as electrode for supercapacitor. Compared with NiFe-LDH/CNFs, NiFe-LDH/CNTs and NiFe-LDH/RGO, NiFe-LDH/RGO/CNFs demonstrated a high specific capacitance of  $1330.2 \text{ F g}^{-1}$  at  $1 \text{ A g}^{-1}$  and a super rate capability of 64.2% from 1 to  $20 \text{ A g}^{-1}$ , indicating great potential for supercapacitor application. Additionally, an asymmetric supercapacitor using NiFe-LDH/RGO/CNFs composite as positive electrode material and activated carbon as negative electrode material was assembled. The asymmetric supercapacitor can work in the voltage range of 0–1.57 V. It displayed high energy density of  $33.7 \text{ W h kg}^{-1}$  at power density of  $785.8 \text{ W kg}^{-1}$  and excellent cycling stability with 97.1% of the initial capacitance after 2500 cycles at  $8 \text{ A g}^{-1}$ . Two flexible AC//LDH-RGO-CNFs ASC devices connected in series were able to light up a red LED indicator after being fully charged. The results demonstrate that the AC//LDH-RGO-CNFs ASC has a promising potential in commercial application.

Over the past few years, supercapacitor (also known as electrochemical capacitor) has attracted intense interest because of their high energy density, excellent cycling stability, environmental friendliness and rapid charge-discharge rate<sup>1–6</sup>. According to the energy storage mechanisms, supercapacitors can generally categorized into electrical double layer capacitor (EDLC) and pseudocapacitor (PC)<sup>7</sup>. It is well known that carbon materials are fundamental candidates for EDLC<sup>8</sup>. Until now, a variety of carbon materials have been used as the electrode materials such as carbon nanotubes (CNTs)<sup>8–10</sup>, carbon nanofibres (CNFs)<sup>11–14</sup>, reduced graphene oxide (RGO) and so on<sup>8,15–17</sup>. Compared with EDLC, PC was major based on transition metal oxides/hydroxides or conducting polymers by redox reactions during charge-discharge processes<sup>8,9,18–20</sup>. It should be noted that, the properties of active electrode materials are the key factors that affect the properties of supercapacitor<sup>21</sup>. Consequently, wonderful electrode materials with high surface area and plenty of activesites are imminently requirement for blossoming electrochemical energy storage and conversion systems<sup>4</sup>.

Layered double hydroxide (LDH), as a family of layered anionic materials, has received considerable attention due to their flexible ion-exchange ability, high specific surface area and flexible structures<sup>5,22,23</sup>. Nevertheless, the relatively low conductivity of LDH often restricts electron transfer and limits the rate of mass diffusion during the redox reaction. Beyond that the agglomeration of LDH may lead to low energy density and limit cycling stability during the charge/discharge processes. As known to all, the electrochemical performances of LDH can be improved effectively when they are combined with carbon materials. As additives, carbon materials can prevent the agglomeration of LDH, improve the specific surface area of the composition and enhance the electrical conductivity of the compound<sup>22,24,25</sup>. To this end, various composites have been produced as high-performance electrode materials of PC. Guan *et al.* reported CoAl-LDH/CNFs can achieve maximum specific capacitance of  $634.3 \text{ F g}^{-1}$  at  $1 \text{ A g}^{-1}$ <sup>26</sup>. Cao *et al.* found that CoNiAl-LDH/RGO (25) exhibited the specific capacitance of  $1866 \text{ F g}^{-1}$  at  $1 \text{ A g}^{-1}$ . Furthermore, the composite displayed wonderful cycling performances without an obvious

Shaanxi Key Laboratory of Natural Products & Chemical Biology, College of Chemistry & Pharmacy, Northwest A&F University, Xinong Road 22, Yangling, Shaanxi, 712100, P.R. China. Correspondence and requests for materials should be addressed to H.L. (email: [hongjuanli@nwfufu.edu.cn](mailto:hongjuanli@nwfufu.edu.cn))

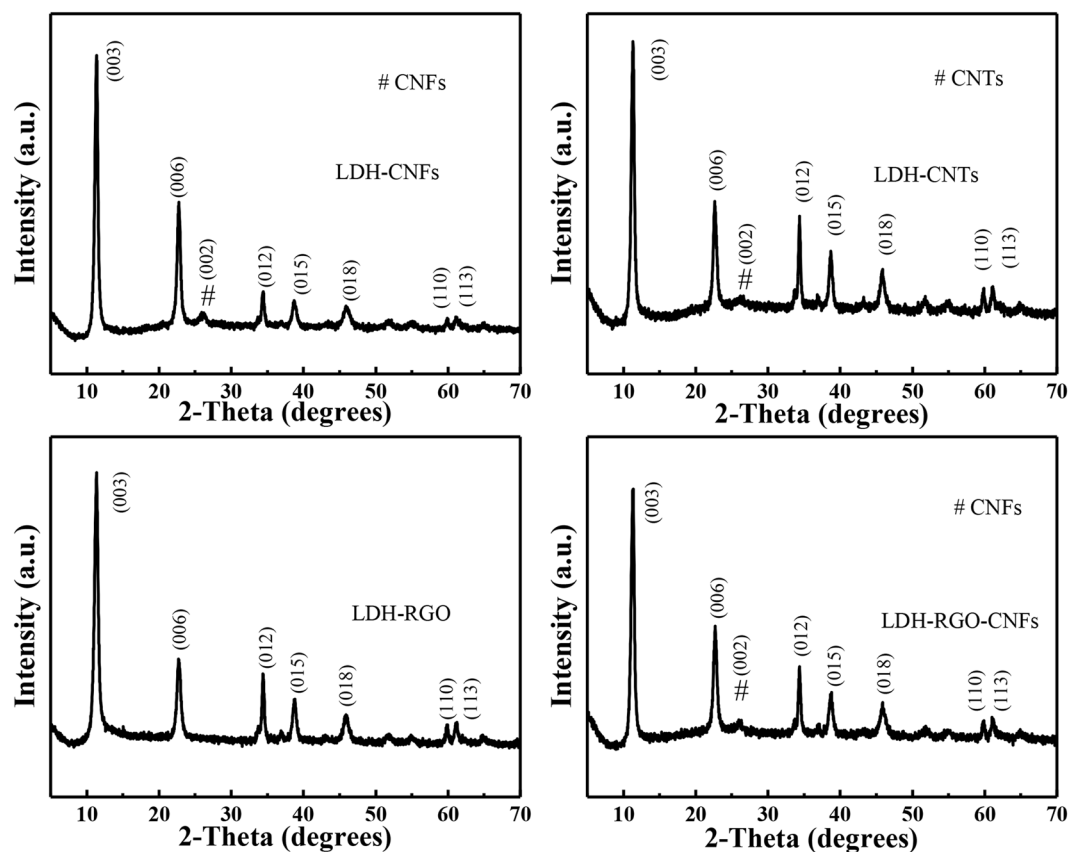


**Figure 1.** XRD spectra of LDH-CNFs, LDH-CNTs, LDH-RGO and LDH-RGO-CNFs.

capacitance decrease after 5000 cycles<sup>27</sup>. Cheng *et al.* prepared the ternary Ni-Mn LDH/CNTs/RGO composite, and the product yielded the specific capacitance of  $1268 \text{ F g}^{-1}$  in  $2 \text{ M KOH}$  electrolyte<sup>28</sup>. Our previous work found that NiFe-LDH material with high crystallinity and well-defined hexagonal shapes was perfect candidate for energy store<sup>29</sup>. However, NiFe-LDH material has always been investigated for water splitting or water oxidation but not often has been evaluated its electrochemical properties for supercapacitor application<sup>23,30</sup>.

In this work, we synthesised NiFe-LDH/CNFs, NiFe-LDH/CNTs, NiFe-LDH/RGO and NiFe-LDH/RGO/CNFs composites for supercapacitor electrodres by a hydrothermal route under mild conditions. Compared with other composites, the NiFe-LDH/RGO/CNFs composite expressed the best electrochemical performance. The composite demonstrated a high specific capacitance of  $1330.2 \text{ F g}^{-1}$  at  $1 \text{ A g}^{-1}$  and a super rate capability of 64.2% from 1 to  $20 \text{ A g}^{-1}$ , indicating great potential for supercapacitor applications. Moreover, an asymmetric supercapacitor using NiFe-LDH/RGO/CNFs composite as positive electrode material and AC as negative electrode material was assembled. The asymmetric supercapacitor showed large energy density of  $33.7 \text{ W h kg}^{-1}$  at power density of  $785.8 \text{ W kg}^{-1}$  and wonderful cycling stability with 97.1% of the initial specific capacitance after 2500 test cycles at  $8 \text{ A g}^{-1}$ , manifesting its promising application in the future.

## Results and Discussion

X-ray diffraction (XRD) is conducted to study the structure of the as-synthesized materials. The XRD patterns of LDH-CNFs, LDH-CNTs, LDH-RGO and LDH-RGO-CNFs are shown in Fig. 1. The diffraction peaks at  $11.3^\circ$ ,  $22.6^\circ$ ,  $34.4^\circ$ ,  $38.7^\circ$ ,  $45.8^\circ$ ,  $59.9^\circ$ , and  $61.0^\circ$  can be assigned to the (003), (006), (012), (015), (018), (110) and (113) planes of the hydroxalcalite-like LDH phase. Furthermore, for LDH-CNFs, LDH-CNTs and LDH-RGO-CNFs, the diffraction peak at  $24.5^\circ$  belong to (002) plane of graphite, demonstrating a successful production of LDH-CNFs, LDH-CNTs and LDH-RGO-CNFs<sup>27,31</sup>. The absence of the peak of RGO in LDH-RGO manifested that the RGO nanosheets were tightly embedded by LDH nanosheets<sup>24,31</sup>.

Moreover, the Raman spectra of CNFs, GO and LDH-RGO-CNFs are shown in Fig. S1. Two major peaks at  $1350$  and  $1580 \text{ cm}^{-1}$  belonged to D and G bands of carbon materials, respectively. D band reflected the defect and the disordered structure of carbon, and G band was attributed to the graphitic in-plane vibrations of ideal  $sp^2$  carbons<sup>31</sup>. In addition, two absorption peaks at  $569.6$  and  $670.2 \text{ cm}^{-1}$  were apparent in the Raman spectrum of LDH-RGO-CNFs, which should be the feature peaks of NiFe-LDH, indicating the coexistence of carbon material and LDH<sup>32,33</sup>.

The chemical bonding nature of the LDH-CNFs, LDH-CNTs, LDH-RGO and LDH-RGO-CNFs was tested by FT-IR spectroscopy, as shown in Fig. 2. The infrared band around  $3460 \text{ cm}^{-1}$  can be assigned to the OH-stretching vibration in the brucite-like layers and interlayer water, accompanied by the band at  $1633 \text{ cm}^{-1}$ <sup>28</sup>.

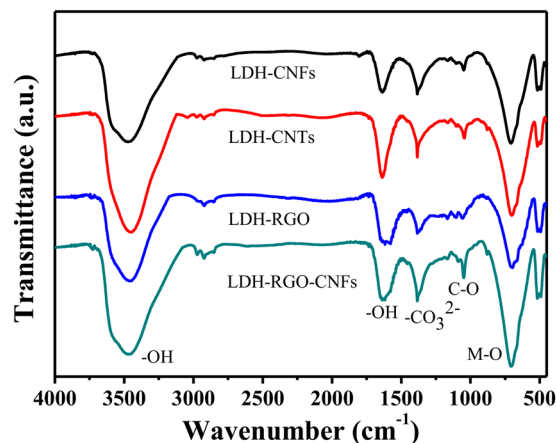


**Figure 2.** FT-IR spectra of LDH-CNFs, LDH-CNTs, LDH-RGO and LDH-RGO-CNFs.

In addition, the band at  $1383\text{ cm}^{-1}$  was ascribed to the vibration of  $\text{CO}_3^{2-}$ <sup>34</sup>. It can be observed that the stretching vibrations of C-O was at  $1049\text{ cm}^{-1}$ <sup>35,36</sup>. Other absorption bands below  $800\text{ cm}^{-1}$  were assigned to metal-oxygen (M-O) stretching and bending vibration in the brucite-like lattice<sup>36</sup>, confirming the existence of NiFe-LDH in the composites.

The morphology and structure of the LDH-CNFs, LDH-CNTs, LDH-RGO and LDH-RGO-CNFs were characterized by FESEM and TEM. As shown in Fig. 3a, the NiFe-LDH displayed the irregular nanoplates and CNFs intercrossed with each other. Therefore, the aggregation of LDH was effectively avoided by introducing CNFs into LDH. From the TEM images of LDH-CNFs (Fig. 3e), the CNFs exhibited a hollow tubular structure with the inner diameter about 100 nm. From Fig. 3b, we can see that the LDH-CNTs was composed of numerous LDH nanosheets and CNTs randomly dispersed on the surfaces of LDH platelets. Compared with CNFs, CNTs (Fig. 3f) showed a smaller diameter, which was not conducive to prevent the aggregation of LDH. As shown in Fig. 3c and g, the LDH nanosheets were disorderly entangled with scrolled and corrugated RGO nanosheets. As expected, the LDH-RGO-CNFs composite (Fig. 3d and h) combined the morphologies of both LDH-CNFs and LDH-RGO. Furthermore, the loose structure of LDH-RGO-CNFs may provide numerous electrochemically active sites and lead to higher specific capacitance. In addition, the incorporation of RGO into LDH can prevent LDH nanosheets from aggregation and improve the specific surface area of the composite. Meanwhile, the CNFs can enhance the electrical conductivity of nanohybrids as a conducting scaffold. The EDS spectra of the LDH-CNFs, LDH-CNTs, LDH-RGO and LDH-RGO-CNFs composites are presented in Fig. S2. The elements of C, O, Ni, Fe, Pt, and Si were detected. The Pt signal came from the plated element for SEM measurement. The peak of Si originated from the silicon slice.

Furthermore, X-ray photoelectron spectroscopy (XPS) was also performed for CNFs, CNTs, GO, and LDH-RGO-CNFs, as shown in Fig. S3 and Fig. 4. Characteristic peaks for C, Ni, Fe and O elements were indicated in the survey spectrum (Fig. 4a). In Fig. 4b, peaks at the binding energy of 855.8 eV and 873.4 eV were related to Ni  $2p_{3/2}$  and Ni  $2p_{1/2}$ , respectively. Moreover, the spin orbit splitting value of Ni  $2p_{3/2}$  and Ni  $2p_{1/2}$  can reach 17.6 eV, indicating that the main oxidation state of Ni is +2<sup>31</sup>. The Fe 2p (Fig. 4c) spectrum showed prominent peaks at 713.9 eV for Fe  $2p_{3/2}$  and 725.5 eV for Fe  $2p_{1/2}$ <sup>37</sup>. As shown in Fig. S3, compared with the C1s spectrum of GO, the intensities of oxygen-containing functional groups were decreased in LDH-RGO-CNFs, confirming the well reduction of GO into RGO<sup>38,39</sup>.

The thermal stability of CNFs, CNTs, GO, and LDH-RGO-CNFs was researched by thermogravimetric analysis (TGA). As shown in Fig. 4d, three significant weight loss stages were observed in the TGA pattern of the LDH-RGO-CNFs. The first weight loss was due to the removal of surface and intercalated water molecules<sup>22</sup>. The second weight loss was the removal of interlayer anions and the de-hydroxylation of LDH crystals<sup>17,40</sup>. The third weight loss was assigned to the the combustion of the carbon skeleton<sup>40</sup>. The residue percentage of the LDH-RGO-CNFs was much higher than CNFs and GO, indicating that the combination of LDH with carbon materials significantly improved the thermal stability.

The electrochemical behavior of LDH-RGO<sub>x</sub>-CNFs ( $X = 0.25, 0.5, 1, 2, 4$ ) composites with different mass ratios of RGO and CNFs were studied by cyclic voltammetry (CV) and galvanostatic charge-discharge (GCD). As shown in Fig. S4, the specific capacitance of LDH-RGO-CNFs ( $1330.2\text{ F g}^{-1}$ ) was superior than LDH-RGO<sub>0.25</sub>-CNFs ( $601.4\text{ F g}^{-1}$ ), LDH-RGO<sub>0.5</sub>-CNFs ( $642.1\text{ F g}^{-1}$ ), LDH-RGO<sub>2</sub>-CNFs ( $743.2\text{ F g}^{-1}$ ) and LDH-RGO<sub>4</sub>-CNFs ( $661.1\text{ F g}^{-1}$ ) at  $1\text{ A g}^{-1}$ . Thus, the LDH-RGO-CNFs was deemed as the best suitable sample for supercapacitor electrode.

In order to evaluate the electrochemical performances of the LDH-CNFs, LDH-CNTs, LDH-RGO and LDH-RGO-CNFs composites, the samples were studied by CV, GCD and EIS. Figure 5a shows the CV curves of the four samples in the 6 M KOH at  $10\text{ mV s}^{-1}$  in a voltage range of 0–0.57 V. All CV curves consisted of a couple of redox peaks, manifesting that the capacitance of the products was mainly associated with faradaic pseudocapacitor. In addition, compared with the LDH-CNFs, LDH-CNTs and LDH-RGO, the LDH-RGO-CNFs exhibited a largest integrated area, indicating the LDH-RGO-CNFs had highest specific capacitance<sup>31</sup>. Figure S5 shows the CV curves of the LDH-CNFs, LDH-CNTs, LDH-RGO and LDH-RGO-CNFs composites at different scan

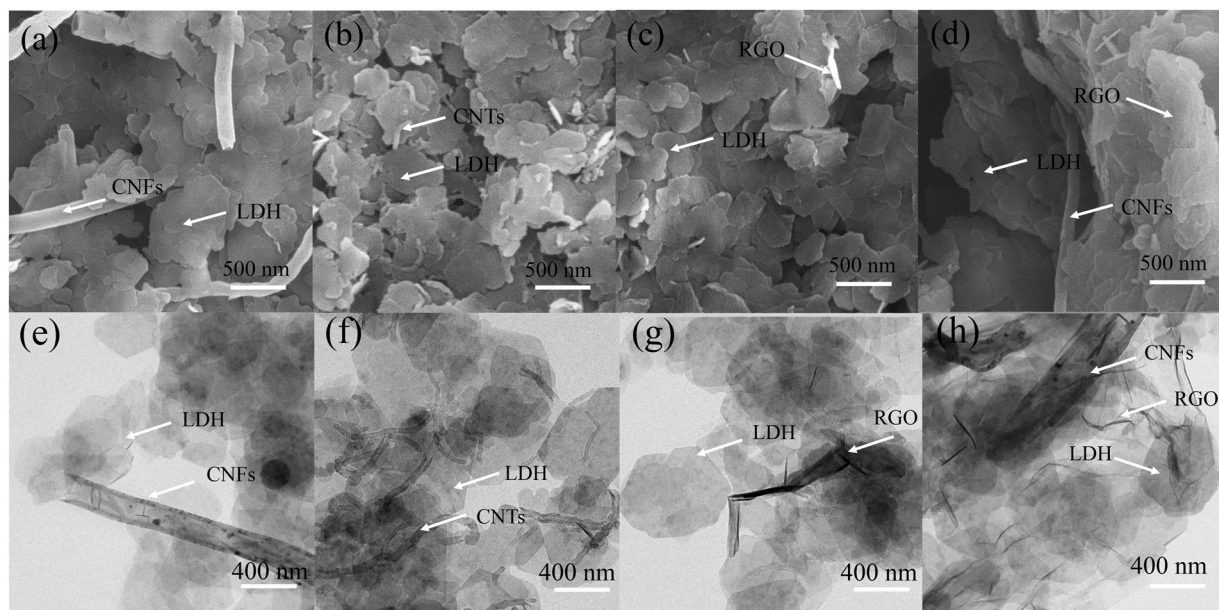


**Figure 3.** FESEM images of (a) LDH-CNFs, (b) LDH-CNTs, (c) LDH-RGO and (d) LDH-RGO-CNFs. TEM images of (e) LDH-CNFs, (f) LDH-CNTs, (g) LDH-RGO and (h) LDH-RGO-CNFs.

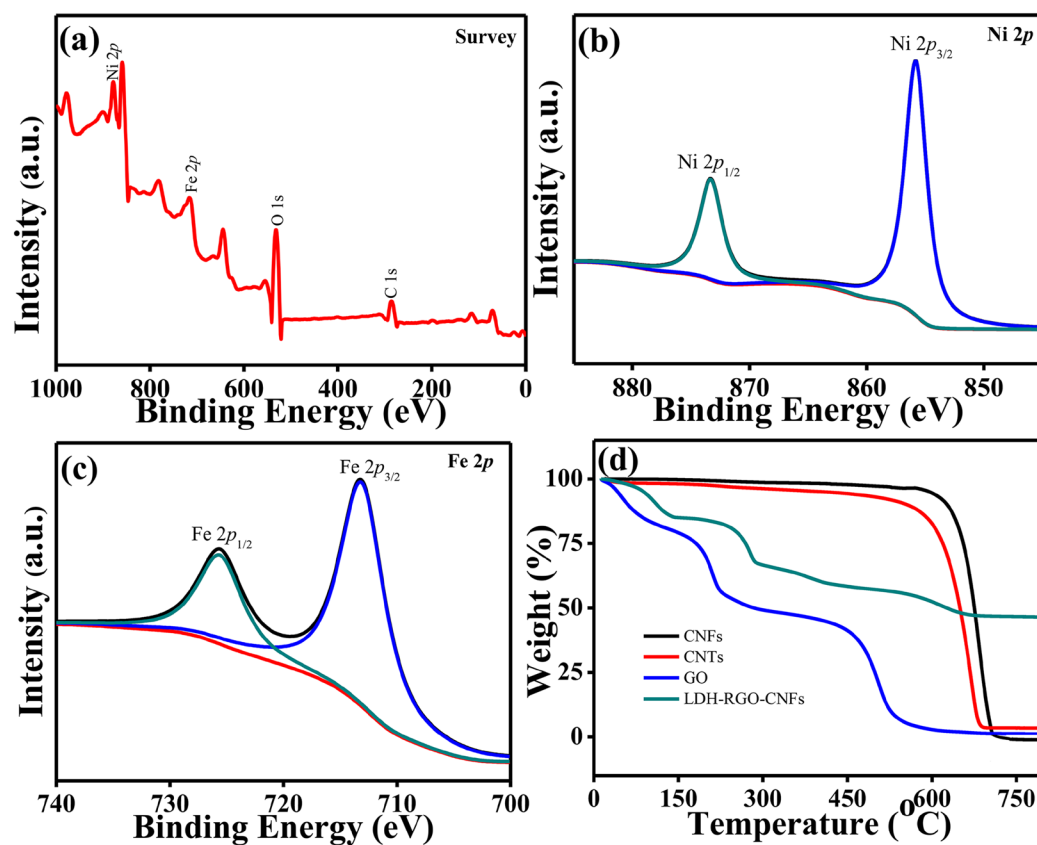


**Figure 4.** XPS survey and high-resolution spectra of LDH-RGO-CNFs. (a) Survey, (b) Ni 2p, (c) Fe 2p; (d) TGA curves of CNFs, CNTs, GO, LDH-RGO-CNFs.

rates. With the increased of the scan rate, the current response also increased without any obvious changes in the shape of the CV, meaning a good rate capability of the active materials<sup>41,42</sup>. Furthermore, the anodic peaks shifted positively and cathodic peaks shifted negatively, respectively, which was mainly due to the internal resistance of electrode<sup>8,43</sup>.

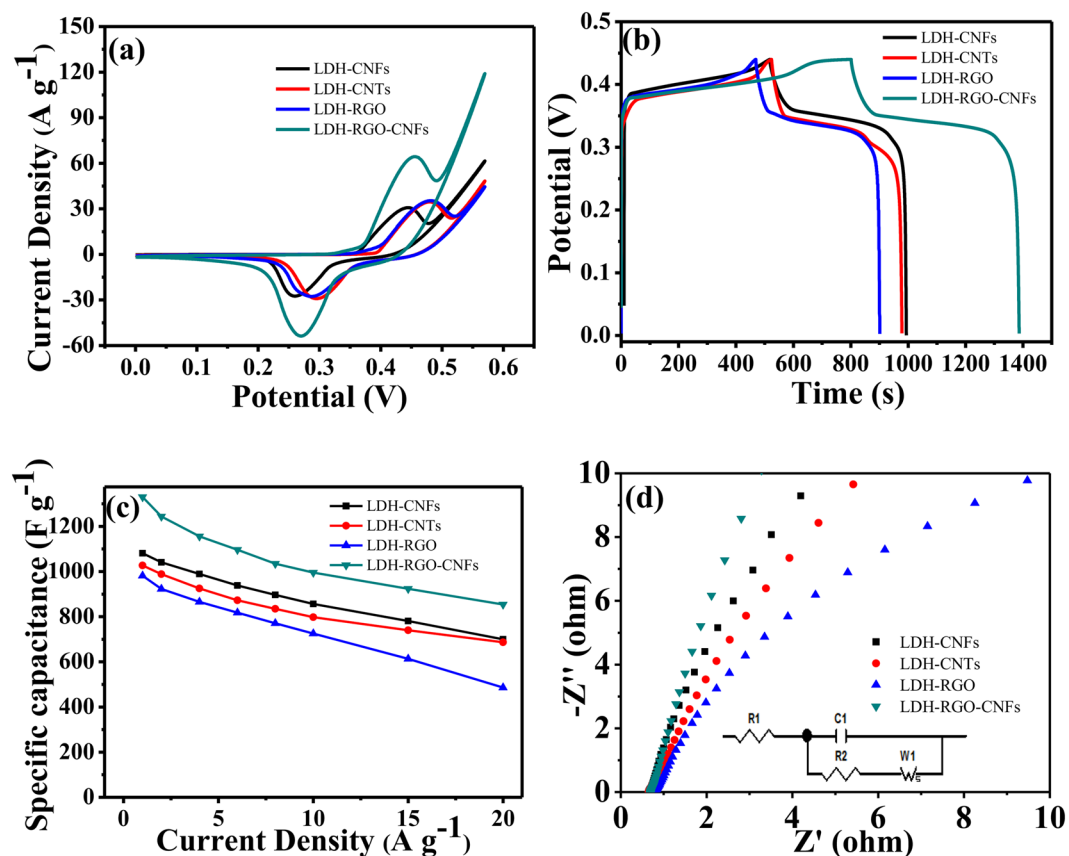


**Figure 5.** Electrochemical capacitive properties of LDH-CNFs, LDH-CNTs, LDH-RGO and LDH-RGO-CNFs composites tested using a three-electrode system in 6M KOH solution. **(a)** CV curves at  $10\ mV\ s^{-1}$ . **(b)** GCD curves at  $1\ A\ g^{-1}$ . **(c)** The specific capacitance at different current densities. **(d)** The Nyquist plots measured at frequency range between  $0.01$  and  $10^5\ Hz$ . Inset: simplified equivalent circuit.

To further illustrate the electrochemical performances of the composites, GCD measurements were conducted. Figure 5b displays the charge/discharge curves of the LDH-CNFs, LDH-CNTs, LDH-RGO and LDH-RGO-CNFs composites at  $1\ A\ g^{-1}$  in a voltage range of  $0-0.44\ V$ . It is clearly seen that the LDH-RGO-CNFs composite demonstrated the longest charge/discharge time, implying the highest specific capacitance. The charge/discharge curves of the LDH-CNFs, LDH-CNTs, LDH-RGO and LDH-RGO-CNFs composites at different current densities are shown in Fig. S6. It showed that the discharge times decreased with the increase of the current density from  $1$  to  $20\ A\ g^{-1}$ . It can be attributed to the limited diffusion rate of the alkali ions. When the current densities increased, the diffusion rate of the alkali ions became relatively low, and thus only the outer active surface of the electrode material can be utilized for charge storage during the redox process<sup>17</sup>. Furthermore, no apparent IR drop was observed in the curves of LDH-RGO-CNFs, meaning that the composite had a low internal resistance. The specific capacitances obtained from GCD tests can be calculated according to eq. (1), as shown in Fig. 5c and Table S1. The outstanding specific capacitances of LDH-RGO-CNFs at  $1, 2, 4, 6, 8, 10, 15, 20\ A\ g^{-1}$  were  $1330.2, 1244.1, 1155.5, 1096.4, 1034.5, 995.5, 923.9$  and  $854.5\ F\ g^{-1}$ , respectively. The retention rate of LDH-RGO-CNFs ( $64.2\%$ ) was larger than those of LDH-RGO ( $49.5\%$ ), LDH-CNTs ( $63.2\%$ ) and LDH-CNFs ( $63.9\%$ ) from  $1$  to  $20\ A\ g^{-1}$ . (Table S1) It can be explained that the introduction of RGO was effectively avoided the aggregation of LDH and prevented the loss of the active surface area of the composite. In addition, adding CNFs not only can effectively increase the electrical conductivity of the composite, but also can improve the spacing of graphene layer, leading to a fast electrolyte ion diffusion path during the charge/discharge processed<sup>42</sup>. Therefore, the electrochemical performances of the LDH-RGO-CNFs composite have been improved.

The electrochemical impedance technique (EIS) was used to investigate the electrochemical performances of the LDH-CNFs, LDH-CNTs, LDH-RGO and LDH-RGO-CNFs composites in a frequency range between  $0.01$  and  $10^5\ Hz$ . The Nyquist plots of the EIS recorded for the composites are shown in Fig. 5d, and the inset shows the simplified equivalent circuit.  $R_e$  represented the resistance related to the ionic conductivity of the electrolyte and electronic conductivity of the electrodes and current collectors<sup>43</sup>, which can be valued by the intercept of a quasi-semicircle in the x axis<sup>42</sup>. The semicircle in the high frequency region represents the charge transfer resistance ( $R_{ct}$ ) at the electrode/electrolyte interface<sup>9</sup>. Evidently, in high frequency area, the  $R_e$  of LDH-RGO-CNFs exhibited a small x axis intercept and a negligible semicircle, indicating a very low internal resistance and charge transfer resistance. Besides, compared with LDH-CNFs, LDH-CNTs and LDH-RGO, LDH-RGO-CNFs had a more vertical line in the low frequency area, confirming a lower Warburg impedance<sup>32</sup>. These results demonstrated that the addition of CNFs and RGO improved the conductivity of the product and decreased the impedance.

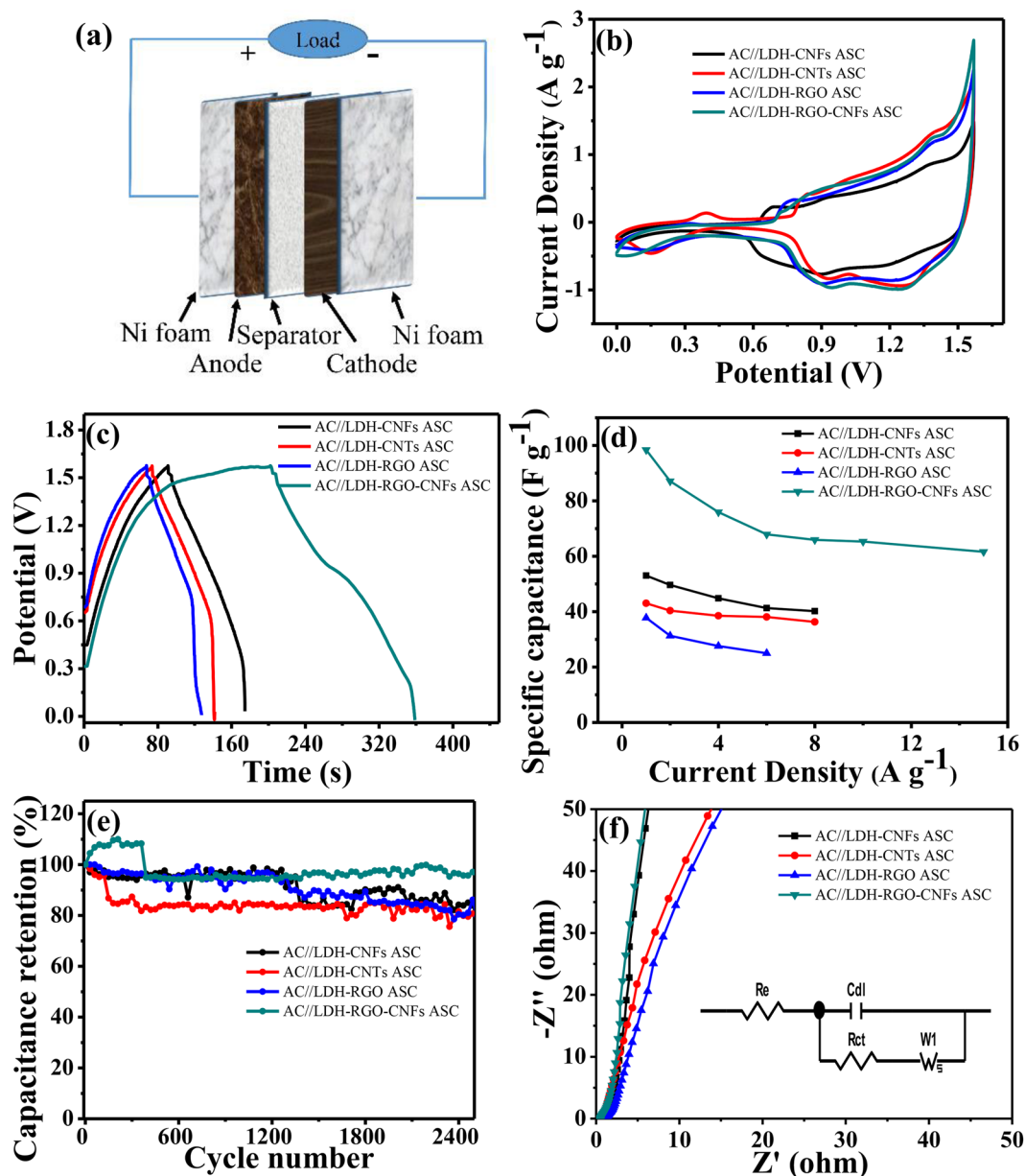


**Figure 6.** (a) The schematic of the ASC. Electrochemical capacitive properties of AC//LDH-CNFs ASC, AC//LDH-CNTs ASC, AC//LDH-RGO ASC and AC//LDH-RGO-CNFs ASC. (b) CV curves at  $10 \text{ mV s}^{-1}$ . (c) GCD curves at  $1 \text{ A g}^{-1}$ . (d) The specific capacitance at different current densities. (e) The specific capacitance retention with 2500 cycling numbers for the AC//LDH-CNFs ASC, AC//LDH-CNTs ASC and AC//LDH-RGO-CNFs ASC at  $8 \text{ A g}^{-1}$  and AC//LDH-RGO ASC at  $6 \text{ A g}^{-1}$ . (f) The Nyquist plots measured in a frequency range between  $0.01$  and  $10^5 \text{ Hz}$ . Inset: simplified equivalent circuit.

To further evaluate the electrochemical properties of the as-prepared composites for practical application, ASCs were assembled by using the as-prepared composites as the positive electrode material and AC as the negative electrode material (Fig. 6a). Figure S7a shows the CV curves of AC and LDH-RGO-CNFs electrodes at  $10 \text{ mV s}^{-1}$ . The AC and LDH-RGO-CNFs electrodes were operated at voltage windows of  $-1.0-0 \text{ V}$  and  $0-0.57 \text{ V}$ , respectively. Therefore, the total cell voltage of the ASC device can be increased up to  $1.57 \text{ V}$ , which was the sum of the voltage range for the AC and LDH-RGO-CNFs electrodes<sup>44</sup>. Figure S7b displays the CV curves of the ASC working at different cell voltages varying from  $0-1 \text{ V}$  to  $0-1.8 \text{ V}$  at  $10 \text{ mV s}^{-1}$ . The CV curves were stable at  $1.57 \text{ V}$ . However, when the voltage was higher than  $1.57 \text{ V}$ , the CV curves exhibited a distortion which can be attributed to some irreversible reactions occurring. Therefore, an operation voltage range of  $1.57 \text{ V}$  was chosen to investigate the electrochemical performances of ASCs. Figure 6b and c shows the CV and GCD curves of AC//LDH-CNFs ASC, AC//LDH-CNTs ASC, AC//LDH-RGO ASC and AC//LDH-RGO-CNFs ASC in the voltage range of  $0-1.57 \text{ V}$ . Clearly, the AC//LDH-RGO ASC exhibited the largest enclosed area of CV curves and longest discharge time of GCD curves, indicating its superior capacitance performance. In addition, Figs S8 and S9 shows

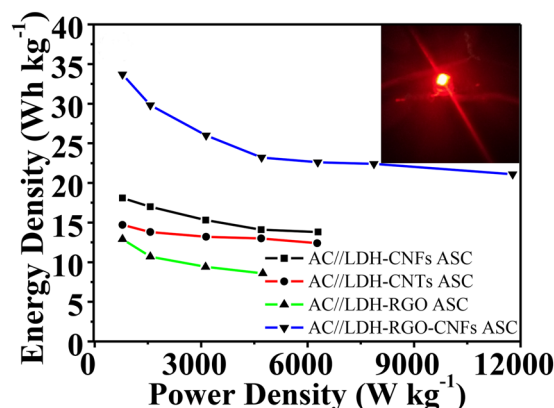


**Figure 7.** Ragone plot of the energy density vs. power density for the ASCs. The inset shows that two AC//LDH-RGO-CNFs ASC devices in series lighting up a red LED indicator.

the CV and GCD curves of four ASCs at different scan rates and current densities, respectively. The results were consistent with the CV and GCD analysis in the three-electrode configuration. Figure 6d and Table S2 displays the specific capacitance of the four ASCs at different current densities. The AC//LDH-RGO-CNFs ASC demonstrated the specific capacitance of 98.4, 87.1, 75.9, 67.9, 65.9, 65.3 and 61.6  $\text{F g}^{-1}$  at 1, 2, 4, 6, 8, 10 and 15  $\text{A g}^{-1}$ , which were higher than those of the other three ASCs at the same current density. In addition, The long-term cycling stability of the four ASCs were tested and the result is shown in Fig. 6e. The capacity of AC//LDH-RGO-CNFs ASC can retain 97.1% of its initial capacity after 2500 consecutive GCD tests at 8  $\text{A g}^{-1}$ , which was better than the capacitance retention of AC//LDH-CNFs ASC (83.9% retention at 8  $\text{A g}^{-1}$ ), AC//LDH-CNTs ASC (80.7% retention at 8  $\text{A g}^{-1}$ ) and AC//LDH-RGO ASC (86.2% retention at 6  $\text{A g}^{-1}$ ). Initial increase of the specific capacitance of the AC//LDH-RGO-CNFs ASC showed an excellent cycling stability at high current density. EIS of the ASCs were measured in a frequency range between 0.01 and  $10^5$  Hz (Fig. 6f). The inset of Fig. 6f shows the simplified equivalent circuit. The  $R_{ct}$  of AC//LDH-RGO-CNFs ASC (0.6  $\Omega$ ) was lower than AC//LDH-CNFs ASC (0.65  $\Omega$ ), AC//LDH-CNTs ASC (0.73  $\Omega$ ) and AC//LDH-RGO ASC (1.36  $\Omega$ ), indicating good charge-transfer conductivity of the device at the electrolyte-electrode interface. Otherwise, AC//LDH-RGO-CNFs ASC exhibited the straight line close to  $90^\circ$  in the low frequency, suggesting a lower Warburg impedance.

Energy density and power density have been widely used to evaluate the performance of the ASCs. According to eqs (3) and (4), the energy density and power density were calculated and shown in Fig. 7. Obviously, the AC//LDH-RGO-CNFs ASC exhibited much higher energy density than the other three ASCs. The maximum energy density of the AC//LDH-RGO-CNFs ASC was 33.7  $\text{Wh Kg}^{-1}$  at the power density of 785.8  $\text{W Kg}^{-1}$ , and still remained at 21.1  $\text{Wh Kg}^{-1}$  at a power density of 11776.6  $\text{W Kg}^{-1}$ . The AC//LDH-RGO-CNFs ASC device displayed improved energy density and power density in aqueous electrolyte solutions compared with many previous reported asymmetric supercapacitors, such as AC//CoMn-LDH /Ni foam ASC (5.9  $\text{Wh Kg}^{-1}$ )<sup>45</sup>, AC//MnO<sub>2</sub>/reclaimed CNFs ASC (22.9  $\text{Wh Kg}^{-1}$ )<sup>46</sup>, AC/CFP//Co(OH)<sub>2</sub>/GNS ASC (19.3  $\text{Wh Kg}^{-1}$ )<sup>47</sup>, AC//NiCo-DH ASC (17.5  $\text{Wh Kg}^{-1}$ )<sup>48</sup>, AC//NiCo-LDH ASC (23.7  $\text{Wh Kg}^{-1}$ )<sup>49</sup>, AEG//CoAl-LDH/GF ASC (28.0  $\text{Wh Kg}^{-1}$ )<sup>36</sup> and AC//Co<sub>3</sub>O<sub>4</sub>-CHCF ASC (24.3  $\text{Wh Kg}^{-1}$ )<sup>50</sup>. It proved that production of LDH-RGO-CNFs composite could be an effective approach in achieving high energy density while retaining power density. Two pieces of flexible AC//LDH-RGO-CNFs ASC devices connected in series were able to light up a red LED indicator (inset in Fig. 7). These results further proved the superiorities of the AC//LDH-RGO-CNFs ASC devices and their great promise for flexible energy storage applications.

## Experimental

**Materials.** All the chemicals were used as received. CNFs were obtained from Sigma-Aldrich. Natural flake graphite (325 mesh) was purchased from Alfa-Aesar Co. CNTs with a diameter of 10–20 nm were purchased from Shenzhen Nanotech Port Co. Ltd.

**Surface modification of CNFs and CNTs and preparation of GO.** GO was produced by modified Hummers method as reported by our previous work<sup>51</sup>. To increased the dispersability in water, the introduction of surficial groups onto the surface of CNFs were carried out according to ref.<sup>11</sup>. The purchased CNFs were stirred in 68% HNO<sub>3</sub> with sonication for 30 min and refluxed at 100 °C overnight. Then, the acid-treated CNFs were washed with deionised water to neutral pH and dried at 80 °C overnight. The negatively charged CNTs were prepared according to the same method.

**Preparation of the NiFe-LDH/carbon composites.** The NiFe-LDH/carbon composites were produced by an easy *in situ* growth approach. Foremost, 40 mg of carbon materials (CNFs, CNTs, GO and a mixture of GO and CNFs with the mass ratio of 1:4, 1:2, 1:1, 2:1 and 4:1) were dispersed in 80 mL of deionised water with ultrasonication for 60 min. Then, Ni(NO<sub>3</sub>)<sub>2</sub>·6H<sub>2</sub>O (0.4653 g) and Fe(NO<sub>3</sub>)<sub>3</sub>·9H<sub>2</sub>O (0.1616 g) were dissolved in the above homogeneous slurry. After ultrasonication for 20 min in air at room temperature, CO(NH<sub>2</sub>)<sub>2</sub> (0.2162 g) and Na<sub>3</sub>C<sub>6</sub>H<sub>5</sub>O<sub>7</sub> (0.0060 g) were added under constant magnetic stirring. Afterwards, the resulted mixture was

transferred into a Teflon-lion stainless steel autoclave and kept at 150 °C for 48 h. After the autoclave was cooled down to room temperature, the collected sample was obtained by vacuum filtration, rinsed with deionised water and alcohol for neutralization and dried at 80 °C overnight. The resultant samples were named as LDH-CNFs, LDH-CNTs, LDH-RGO, LDH-RGO<sub>x</sub>-CNFs (X = 0.25, 0.5, 1, 2, 4).

**Material characterization.** The crystalline structures of the samples were analyzed by X-ray diffraction (XRD, D/Max2550VB+/PC X-ray, Cu K $\alpha$ , 0.15406 nm). FESEM (Zeiss Merlin) and TEM (JEM-2100) was used to observe the microstructures of the material. Fourier transform infrared (FT-IR) spectra was obtained on a Bruker EQUINX55 FT-IR spectrophotometer by a standard KBr disk method in the range 400–4000 cm<sup>-1</sup>. Chemical valence states and elemental composition of the samples were analysed by X-ray photoelectron spectroscopy (XPS, Escalab 250Xi, UA). Raman spectrum was performed on a RENISHAW. Thermogravimetric analysis (TGA, NETZSCH, STA 449 F3) was performed in a temperature range from 20 to 800 °C with the heating rate of 10 °C min<sup>-1</sup> in air.

**Preparation of the electrodes.** The obtained sample, acetylene black and polyvinylidene fluoride with a weight ratio of 80:15:5 were mixed and dispersed in ethanol to form homogeneous slurries<sup>15</sup>. Then, the slurries was coated onto a piece of Ni foam and dried at 80 °C overnight to form the working electrode. The resulting electrode was pressed at a pressure of 10 MPa before use.

**Electrochemical measurements.** The electrochemical tests of various samples were conducted using a three electrode system in a solution of 6 M KOH with electrochemical workstation (CHI 660E, Chenhua, Shanghai). Hg/HgO electrode and Pt plate were used as the reference electrode and counter electrode, respectively. A salt-bridge was used to connect Hg/HgO electrode and electrolyte. Cyclic voltammetry (CV) in the range of 0–0.57 V was performed at various scan rates. Galvanostatic charge/discharge (GCD) were recorded in the potential range of 0–0.44 V at different current densities. Electrochemical impedance spectroscopy (EIS) was tested in the frequency range between 0.01 and 10<sup>5</sup> Hz at the open circuit voltage with an alternating amplitude of 5 mV. Cycle-life test was measured by a battery test system (LAND CT2001A). Asymmetric supercapacitors (ASCs) were produced with NiFe-LDH/carbon materials and activated carbon (AC) as positive electrode and negative electrode, respectively. The electrolyte was 6 M KOH. The negative electrode was fabricated by the similar procedure. The specific capacitance of a single electrode was calculated from the charge/discharge curve according to the following equations<sup>15</sup>:

$$C_s = \frac{I \times t}{\Delta V \times m} \quad (1)$$

herein,  $C_s$  (F g<sup>-1</sup>) is specific capacitance,  $I$  (A) is the discharge current,  $\Delta t$  (s) is the discharge time,  $m$  (g) is the mass of the sample coated on the Ni foam surface and  $\Delta V$  (V) is the discharge voltage range.

To achieve optimal electrochemical performance, the mass ratio of positive and negative electrode is received according to eq. (2):

$$\frac{m_+}{m_-} = \frac{C_- \times \Delta V_-}{C_+ \times \Delta V_+} \quad (2)$$

herein,  $m$  (g) is the mass loading,  $C$  (F g<sup>-1</sup>) is the specific capacitance,  $\Delta V$  (V) is the discharge voltage range for the positive (+) and negative (–) electrodes.

The energy density and power density of the ASCs were calculated according to eqs (3) and (4), respectively:

$$E = \frac{1}{2} C_s \Delta V^2 \quad (3)$$

$$P = \frac{E \times 3600}{t} \quad (4)$$

herein,  $E$  (W h kg<sup>-1</sup>) is energy density,  $P$  (W h kg<sup>-1</sup>) is power density,  $C_s$  (F g<sup>-1</sup>) is specific capacitance,  $\Delta V$  (V) is the discharge voltage range and  $\Delta t$  (s) is the discharge time.

## Summary

In summary, we have successfully synthesized the LDH-CNFs, LDH-CNTs, LDH-RGO and LDH/RGO/CNFs composites with a facile one-step hydrothermal method, and studied their electrochemical properties in three and two electrode systems. The LDH/RGO/CNFs composite exhibited the highest specific capacitance of 1330.2 F g<sup>-1</sup> at 1 A g<sup>-1</sup> in three electrode systems. An asymmetric supercapacitor was fabricated by the LDH/RGO/CNFs composite as positive electrode and AC as negative electrode. The AC//LDH-RGO-CNFs ASC could operate at a wide voltage range of 0–1.57 V, delivered a large energy density of 33.7 W h kg<sup>-1</sup> at power density of 785.8 W kg<sup>-1</sup> and showed a remarkable cycling stability with 97.1% of the initial capacitance after 2500 cycles at 8 A g<sup>-1</sup>. Notably, two flexible AC//LDH-RGO-CNFs ASC devices connected in series were able to light up a red LED indicator after being fully charged. The remarkable electrochemical performances indicated that the LDH-RGO-CNFs composite was a promising electrode material and had great application potential for energy storage.



## References

- Zhang, L. *et al.* 3D porous layered double hydroxides grown on graphene as advanced electrochemical pseudocapacitor materials. *J. Mater. Chem. A* **1**, 9046–9053 (2013).
- Gu, Y. *et al.* NiTi layered double hydroxide thin films for advanced pseudocapacitor electrodes. *J. Mater. Chem. A* **1**, 10655–10661 (2013).
- Hao, X. *et al.* Engineering one-dimensional and two-dimensional birnessite manganese dioxides on nickel foam-supported cobalt-aluminum layered double hydroxides for advanced binder-free supercapacitors. *RSC Adv.* **4**, 63901–63908 (2014).
- Shao, M. *et al.* Layered double hydroxides toward electrochemical energy storage and conversion: design, synthesis and applications. *Chem. commun.* **51**, 15880–15893 (2015).
- Chen, S. *et al.* A high-rate cathode material hybridized by *in-situ* grown Ni-Fe layered double hydroxides and carbon black nanoparticles. *J. Mater. Chem. A* **4**, 4877–4881 (2016).
- Zheng, X., Gu, Z., Hu, Q., Geng, B. & Zhang, X. Ultrathin porous nickel-cobalt hydroxide nanosheets for high-performance supercapacitor electrodes. *RSC Adv.* **5**, 17007–17013 (2015).
- Wei, Y. *et al.* Carbon quantum dots/Ni-Al layered double hydroxide composite for high-performance supercapacitors. *RSC Adv.* **6**, 39317–39322 (2016).
- Chen, X. A., Chen, X., Zhang, F., Yang, Z. & Huang, S. One-pot hydrothermal synthesis of reduced graphene oxide/carbon nanotube/ $\alpha$ -Ni(OH)<sub>2</sub> composites for high performance electrochemical supercapacitor. *J. Power Sources* **243**, 555–561 (2013).
- Shen, J., Yang, C., Li, X. & Wang, G. High-performance asymmetric supercapacitor based on nano architected polyaniline/graphene/carbon nanotube and activated graphene electrodes. *ACS Appl. Mater. Interfaces* **5**, 8467–8476 (2013).
- Yang, J. *et al.* Facile fabrication of MWCNT-doped NiCoAl-layered double hydroxide nanosheets with enhanced electrochemical performances. *J. Mater. Chem. A* **1**, 1963–1968 (2013).
- He, F. *et al.* *In situ* fabrication of nickel aluminum-layered double hydroxide nanosheets/hollow carbon nanofibers composite as a novel electrode material for supercapacitors. *J. Power Sources* **267**, 188–196 (2014).
- Warsi, M. F. *et al.* Conformal Coating of Cobalt-Nickel Layered Double Hydroxides Nanoflakes on Carbon Fibers for High-performance Electrochemical Energy Storage Supercapacitor Devices. *Electrochim. Acta* **135**, 513–518 (2014).
- Zhao, J. *et al.* CoMn-layered double hydroxide nanowalls supported on carbon fibers for high-performance flexible energy storage devices. *J. Mater. Chem. A* **1**, 8836–8843 (2013).
- Zhao, J. *et al.* Flexible hierarchical nanocomposites based on MnO<sub>2</sub> nanowires/CoAl hydrotalcite/carbon fibers for high-performance supercapacitors. *RSC Adv.* **3**, 1045–1049 (2013).
- Chen, J., Wang, X., Wang, J. & Lee, P. S. Sulfidation of NiMn-Layered Double Hydroxides/Graphene Oxide Composites toward Supercapacitor Electrodes with Enhanced Performance. *Adv. Energy Mater.* **6**, 1501745–1501752 (2016).
- Ge, X. *et al.* Periodic stacking of 2D charged sheets: Self-assembled superlattice of Ni-Al layered double hydroxide (LDH) and reduced graphene oxide. *Nano Energy* **20**, 185–193 (2016).
- Li, M., Cheng, J. P., Liu, F. & Zhang, X. B. 3D-architected nickel-cobalt-manganese layered double hydroxide/reduced graphene oxide composite for high-performance supercapacitor. *Chem. Phys. Lett.* **640**, 5–10 (2015).
- Chen, Z. *et al.* High-performance supercapacitors based on intertwined CNT/V<sub>2</sub>O<sub>5</sub> nanowire nanocomposites. *Adv. Mater.* **23**, 791–795 (2011).
- Xu, K. *et al.* Hierarchical mesoporous NiCo<sub>2</sub>O<sub>4</sub>@MnO<sub>2</sub> core-shell nanowire arrays on nickel foam for aqueous asymmetric supercapacitors. *J. Mater. Chem. A* **2**, 4795–4802 (2014).
- Tang, C., Tang, Z. & Gong, H. Hierarchically Porous Ni-Co Oxide for High Reversibility Asymmetric Full-Cell Supercapacitors. *J. Chem. Soc.* **159**, A651–A656 (2012).
- Liu, M. *et al.* Eco-friendly synthesis of hierarchical ginkgo-derived carbon nanoparticles/NiAl-layered double hydroxide hybrid electrodes toward high-performance supercapacitors. *RSC Adv.* **5**, 55109–55118 (2015).
- Li, M., Cheng, J. P., Wang, J., Liu, F. & Zhang, X. B. The growth of nickel-manganese and cobalt-manganese layered double hydroxides on reduced graphene oxide for supercapacitor. *Electrochim. Acta* **206**, 108–115 (2016).
- Tang, D. *et al.* Carbon quantum dot/NiFe layered double-hydroxide composite as a highly efficient electrocatalyst for water oxidation. *ACS Appl. Mater. Interfaces* **6**, 7918–7925 (2014).
- Yu, C. *et al.* Nanohybrids from NiCoAl-LDH coupled with carbon for pseudocapacitors: understanding the role of nano-structured carbon. *Nanoscale* **6**, 3097–3104 (2014).
- Memon, J. *et al.* Synthesis of graphene/Ni-Al layered double hydroxide nanowires and their application as an electrode material for supercapacitors. *J. Mater. Chem. A* **2**, 5060–5067 (2014).
- Jagadale, A. D. *et al.* Binder-Free Electrodes of CoAl Layered Double Hydroxide on Carbon Fibers for All-Solid-State Flexible Yarn Supercapacitors. *Energy Technol.* **4**, 997–1004 (2016).
- Huang, P. *et al.* One-pot synthesis of sandwich-like reduced graphene oxide@CoNiAl layered double hydroxide with excellent pseudocapacitive properties. *J. Mater. Chem. A* **3**, 10858–10863 (2015).
- Li, M., Liu, F., Zhang, X. B. & Cheng, J. P. A comparative study of Ni-Mn layered double hydroxide/carbon composites with different morphologies for supercapacitors. *Phys. chem. chem. phys.* **18**, 30068–30078 (2016).
- Li, H., Zhu, G., Liu, Z.-H., Yang, Z. & Wang, Z. Fabrication of a hybrid graphene/layered double hydroxide material. *Carbon* **48**, 4391–4396 (2010).
- Hou, Y. *et al.* Vertically oriented cobalt selenide/NiFe layered-double-hydroxide nanosheets supported on exfoliated graphene foil: an efficient 3D electrode for overall water splitting. *Energy Environ. Sci.* **9**, 478–483 (2016).
- Cai, X. *et al.* Solvothermal synthesis of NiCo-layered double hydroxide nanosheets decorated on RGO sheets for high performance supercapacitor. *Chem. Eng. J.* **268**, 251–259 (2015).
- Yang, W. *et al.* Solvothermal one-step synthesis of Ni-Al layered double hydroxide/carbon nanotube/reduced graphene oxide sheet ternary nanocomposite with ultrahigh capacitance for supercapacitors. *ACS Appl. Mater. Interfaces* **5**, 5443–5454 (2013).
- Gao, Z. *et al.* Graphene Nanosheet/Ni<sup>2+</sup>/Al<sup>3+</sup> Layered Double Hydroxide Composite as a Novel Electrode for a Supercapacitor. *Chem. Mater.* **23**, 3509–3516 (2011).
- Xu, J. *et al.* A sandwich-type three-dimensional layered double hydroxide nanosheet array/graphene composite: fabrication and high supercapacitor performance. *J. Mater. Chem. A* **2**, 1022–1031 (2014).
- Woo, M. A. *et al.* Mixed valence Zn-Co-layered double hydroxides and their exfoliated nanosheets with electrode functionality. *J. Mater. Chem.* **21**, 4286–4292 (2011).
- Masikhwa, T. M. *et al.* High performance asymmetric supercapacitor based on CoAl-LDH/GF and activated carbon from expanded graphite. *RSC Adv.* **6**, 46723–46732 (2016).
- Lu, Y. *et al.* An investigation of ultrathin nickel-iron layered double hydroxide nanosheets grown on nickel foam for high-performance supercapacitor electrodes. *J. Alloy Compd.* **714**, 63–70 (2017).
- Bai, X. *et al.* Nickel-Cobalt Layered Double Hydroxide Nanowires on Three Dimensional Graphene Nickel Foam for High Performance Asymmetric Supercapacitors. *Electrochim. Acta* **215**, 492–499 (2016).
- Beidaghi, M. & Wang, C. Micro-Supercapacitors Based on Interdigital Electrodes of Reduced Graphene Oxide and Carbon Nanotube Composites with Ultrahigh Power Handling Performance. *Adv. Funct. Mater.* **22**, 4501–4510 (2012).
- Garcia-Gallastegui, A. *et al.* Layered double hydroxides supported on multi-walled carbon nanotubes: preparation and CO<sub>2</sub> adsorption characteristics. *J. Mater. Chem.* **22**, 13932–13940 (2012).

41. Zhu, G. *et al.* Highly conductive three-dimensional MnO<sub>2</sub>-carbon nanotube-graphene-Ni hybrid foam as a binder-free supercapacitor electrode. *Nanoscale* **6**, 1079–1085 (2014).
42. Xiong, C. *et al.* Two-step approach of fabrication of interconnected nanoporous 3D reduced graphene oxide-carbon nanotube-polyaniline hybrid as a binder-free supercapacitor electrode. *J. Alloy Compd.* **695**, 1248–1259 (2017).
43. Wang, Y. *et al.* The synthesis and electrochemical performance of core-shell structured Ni-Al layered double hydroxide/carbon nanotubes composites. *Electrochim. Acta* **222**, 185–193 (2016).
44. Zhou, P. *et al.* Facile hydrothermal synthesis of NiTe and its application as positive electrode material for asymmetric supercapacitor. *J. Alloy Compd.* **685**, 384–390 (2016).
45. Jagadale, A. D. *et al.* Ultrathin nanoflakes of cobalt-manganese layered double hydroxide with high reversibility for asymmetric supercapacitor. *J. Power Sources* **306**, 526–534 (2016).
46. Zhao, C. *et al.* Solar-assisting pyrolytically reclaimed carbon fiber and their hybrids of MnO<sub>2</sub>/RCF for supercapacitor electrodes. *Carbon* **114**, 230–241 (2017).
47. Zhao, C. *et al.* A high-performance asymmetric supercapacitor based on Co(OH)<sub>2</sub>/graphene and activated carbon electrodes. *Journal of Electroanalytical Chemistry* **782**, 98–102 (2016).
48. Jing, M. *et al.* Alternating Voltage Introduced NiCo Double Hydroxide Layered Nanoflakes for an Asymmetric Supercapacitor. *ACS Appl. Mater. Interfaces* **7**, 22741–22744 (2015).
49. Wang, X., Sumboja, A., Lin, M., Yan, J. & Lee, P. S. Enhancing electrochemical reaction sites in nickel-cobalt layered double hydroxides on zinc tin oxide nanowires: a hybrid material for an asymmetric supercapacitor device. *Nanoscale* **4**, 7266–7272 (2012).
50. Liu, W., Fan, H., Shen, W. & Qu, S. Facile and Sustainable Synthesis of Co<sub>3</sub>O<sub>4</sub>@Hollow-Carbon-Fiber for a Binder-Free Supercapacitor Electrode. *ChemistrySelect* **1**, 6469–6475 (2016).
51. Li, H. *et al.* Facile synthesis of a nanocomposite based on graphene and ZnAl layered double hydroxides as a portable shelf of a luminescent sensor for DNA detection. *RSC Adv.* **5**, 9341–9347 (2015).

## Acknowledgements

This work was supported by the Fundamental Research Funds for the Central Universities (No. 2452015426); Open Project of Key Laboratory of Applied Surface and Colloid Chemistry (No. 2014012) and Shaanxi Province Science and Technology (No. 2015JQ2057).

## Author Contributions

Hongjuan Li convinced the idea of the research; Feifei Wang and Ting Wang performed the experiments and wrote the manuscript. All authors contributed to the general discussion.

## Additional Information

**Supplementary information** accompanies this paper at <https://doi.org/10.1038/s41598-018-27171-0>.

**Competing Interests:** The authors declare no competing interests.

**Publisher's note:** Springer Nature remains neutral with regard to jurisdictional claims in published maps and institutional affiliations.



**Open Access** This article is licensed under a Creative Commons Attribution 4.0 International License, which permits use, sharing, adaptation, distribution and reproduction in any medium or format, as long as you give appropriate credit to the original author(s) and the source, provide a link to the Creative Commons license, and indicate if changes were made. The images or other third party material in this article are included in the article's Creative Commons license, unless indicated otherwise in a credit line to the material. If material is not included in the article's Creative Commons license and your intended use is not permitted by statutory regulation or exceeds the permitted use, you will need to obtain permission directly from the copyright holder. To view a copy of this license, visit <http://creativecommons.org/licenses/by/4.0/>.

© The Author(s) 2018